PREDICTION OF THE CRITICAL DISTRIBUTED ROUGHNESS HEIGHT INDUCING TRANSITION ON THE EXPERT VEHICLE

Guillaume Grossir, Sébastien Paris, Olivier Chazot, and Patrick Rambaud

von Karman Institute for Fluid Dynamics, 1640 Rhode Saint Genèse, Belgium

ABSTRACT

Distributed roughness elements are applied onto the nose of a scaled model of the EXPERT vehicle to represent an oxidation of the material that would appear during the reentry. The study focuses at Mach 14 corresponding to the peak heating condition along the reentry trajectory. The critical height for distributed roughness elements that would trigger boundary layer transition is obtained from wind-tunnel experiments. These results are compared to predictions from empirical correlations. The correlations with the best agreement to experimental results are used for flight extrapolation. The largest distributed roughness height allowable for flight conditions without triggering transition is determined on this basis.

Key words: hypersonic; boundary layer transition; heat transfer; distributed roughness; correlations; flight extrapolation.

NOMENCLATURE

Symbols

C_H Stanton number
c_p specific heat at constant pressure, J/(kg.K)
k roughness height, m
$\overline{k}$ mean value of roughness height distribution, m
M   Mach number
p pressure, Pa
Pr   Prandtl number
$\dot{Q}$ wall heat flux, W/m^2
r recovery factor
Re   Reynolds number
R_N nosetip radius, m
T temperature, K
U flow velocity, m/s
δ boundary layer thickness, m
μ flow viscosity, Pa.s
ρ flow density, kg/m^3
θ momentum thickness, m

Subscripts

0   stagnation conditions
∞ free-stream conditions
aw   adiabatic wall
e   at the edge of the boundary layer
k   at the height k
L   based on vehicle length L
r   recovery
tr   at transition location
w   at the wall
x   based on length x

1. INTRODUCTION

Transition between laminar and turbulent boundary layers in hypersonic flows induces large changes regarding to the effect on surface heat transfer rates, extent of shock boundary layer interaction, flow separation and control effectiveness and many others.

The EXPERT vehicle (European eXPErimental Re-entry Testbed) is a reentry demonstrator which will experience laminar to turbulent boundary layer transition phenomenon. The re-entry trajectory followed by the vehicle is depicted in Fig. 1 with the evolution of the Reynolds number and stagnation heat flux as a function of the Mach number. Mach and Reynolds similarity parameters can be duplicated in the Longshot facility at a specific point on the reentry trajectory close to peak heating experienced by the vehicle. Therefore, there is the opportunity to conduct experiments at this specific Mach number and to evaluate the influence of disturbing elements. The objective of the present work is to focus on the effects of transition due to distributed roughness on the nose of the vehicle (made of Carbon-Silicon carbide CSiC) which can suffer passive or active oxidation during the re-entry.

The effects of roughness on hypersonic blunt vehicles have been reviewed recently in [11] regarding to both isolated and distributed roughness elements. All kinds of roughness induce early boundary layer transition, and as a general rule: the larger the roughness elements, the smaller the critical Reynolds number. The different mechanisms by which a roughness can induce transition
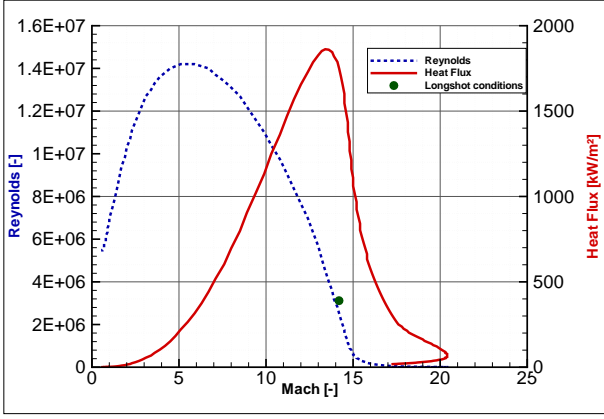
Figure 1. Reentry trajectory of the EXPERT vehicle and comparison with Longshot conditions

are poorly known so far and especially in the case of distributed roughness because of the statistical nature of the roughness elements and their relative interactions. A full geometrical characterization of the roughness elements is not possible as noted in [12].

2. PREVIOUS TRANSITION STUDIES

Studies of transition due to distributed roughness on hypersonic vehicles have first been initiated with the Passive Nosetip Technology (PANT) program. Since it has been the only source of detailed data for many years, several attempts to correlate the results according to different parameters have led to several correlations reviewed in [8]. The one of Anderson and often referred to as PANT's correlation is given in Eq. 1.

$$[\mathrm{Re}_\theta]_{tr} = 215 \left[\frac{k}{\theta} \frac{T_e}{T_w} \right]^{-0.7} \tag{1}$$

The correlation of van Driest (Eq. 2), mentioned in [8], is also based on PANT data but uses a pressure correction term to take into account the effects of stabilizing pressure gradients on curved surfaces.

$$[\mathrm{Re_k}]_{tr} = 200 \left[1 + 0.9 \left(\frac{T_w}{T_e} - 1 \right) + 0.048 \mathrm{M}_e^2 \right]$$
$$\times \underbrace{\left[1 + 350 \left(\frac{k}{R_N} \right) \right]}_{\text{pressure correction term}} \tag{2}$$

Dirling's correlation [4] has been proved to correlate with the best agreement PANT data and is thus believed to be the best one to represent the physics of transition on blunt bodies and hence to predict it. The correlation, as given

in Eq. 3, uses undisturbed flow field properties at the height k of the roughness. A pressure correction term modifying the apparent size of the roughness can also be used according to $k = \overline{k} / \left(1 + 350 \frac{\overline{k}}{R_N} \right)$ where k is the equivalent roughness height, and $\overline{k}$ is the physical average of the roughness heights. If this correction is applied, the constant C in Eq. 3 is equal to 150, otherwise a value of 200 is advised [8].

$$\left[\frac{\rho_k U_k k}{\mu_w} \right]_{tr} = C \tag{3}$$

In [1], additional data sets have been correlated according to Eq. 4 which also uses a pressure correction term. In [9], this correlation is shown to be taken with care since incorrect transformation have been applied between the roughness heights measured in a plane and the equivalent 3-dimensional roughness.

$$[Re_\theta]_{tr} = \begin{cases} 500 X^{-1.5} & 1 \le X \le 10 \\ 500 & X < 1 \end{cases} \tag{4}$$

where $X = \frac{k}{\theta} \frac{T_e}{T_w} \frac{1}{1 + 350 k / R_N}$.

In his review of 2002 [9], Reda uses a correlation similar to the one of Dirling (Eq. 3) for cases where flow properties at the roughness height are unknown. The correlation reads $[\rho_e U_e k / \mu_e]_{tr} = 106$ and uses edge properties.

An interesting correlation (because developed for a blunt slender cone geometry similar to the one of the EXPERT model) has been reported in [3]. The experiments were aiming at triggering transition with distributed roughness elements while keeping the protrusion of the elements as small as possible. Unfortunately for the present application, the correlation relies on distributed roughness extending over a long distance from the nosetip (5 times the curvature radius of the nose) which is not the case for the EXPERT vehicle.

More recently, a correlation based on transient growth theory aiming at explaining early transition on blunt bodies has been published [10]. No curvature correction factor is considered. The correlation is given in Eq. 5.

$$[\mathrm{Re}_\theta]_{tr} = 180 \left(\frac{k}{\theta} \right)^{-1} \left(\frac{T_e}{2T_w} \right)^{-1.27} \tag{5}$$

The numerical factor of 180 is defined for cases where $T_w / T_{aw} = 0.5$. For the experiments reported herein, this ratio was close to 0.5 at the junction between the nose and the conical part of the vehicle while closer to 0.2 at the stagnation point.

One must stress on the fact that all correlations are strongly limited by the number of parameters taken into account to describe the flow field and the roughness parameters. As a consequence, correlations results might

be applicable only to geometries and test conditions similar to the ones for which they were developed. None of them was using a geometry close to the EXPERT one and results must then be considered carefully.

3. EXPERIMENTAL SETUP

3.1. Longshot facility

The Longshot is a low-enthalpy hypersonic piston gun tunnel described in [13]. It is equipped with a contoured Mach 14 nozzle with an exit diameter of $430\,\mathrm{mm}$ for the present experiments. The test gas is nitrogen. Test times of the order of $20\,\mathrm{ms}$ are achieved. Due to the finite volume of the reservoir and mass flow through the nozzle, the total conditions are decaying with time. Reynolds numbers $\mathrm{Re_L}$ are varying between $4\,000\,000$ and $2\,500\,000$ during an experiment.

3.2. Model

The model used is a scaled model of the EXPERT vehicle with $228.7\,\mathrm{mm}$ long. The model is manufactured in Aluminum and mounted on a sting at the exit of the nozzle. It is set at $0\,° \pm 20\,''$ angle of attack and yaw for all experiments. The model is displayed in Fig. 2 with its instrumentation.
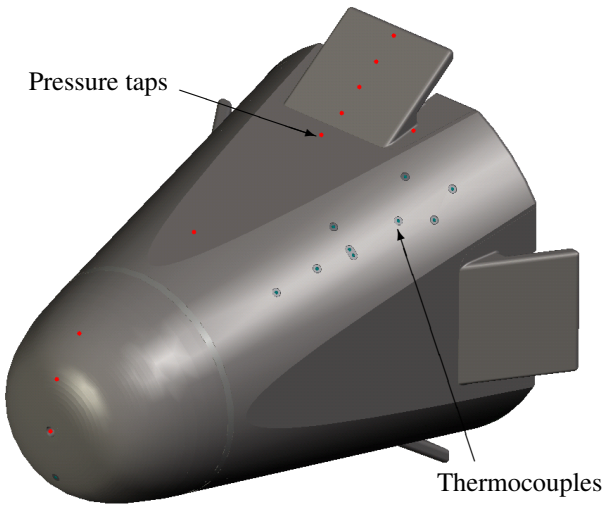

Figure 2. EXPERT model used for the experiments with thermocouples visible on the cone side and pressure taps on the flap side

3.3. Test matrix

The different experiments performed varying the location of the roughness, their size and their densities are summarized in Tab. 1 with their test conditions.

3.4. Instrumentation

The facility is equipped with a fast-response pressure transducer (Kistler 6215) in the reservoir measuring the total pressure. Stagnation pressure and stagnation temperature are measured at the nozzle exit.

The model is further equipped with 21 thermocouples and 11 pressure sensors distributed on the cone side and on the flap side.

Flush mounted coaxial thermocouples are used to measure the transient temperatures at the surface of the model. They are calibrated using a linear law close to the standard values for type-E thermocouples. Wall heat fluxes are determined after two assumptions as described in [13]: the heat flux is one-dimensional, and the wall is semi-infinite. The first assumption is valid if the thermal properties of the thermocouple and the surrounding material are the same (no radial conduction). Thus, thermocouples are mounted within Chromel inserts whose thermal properties are close. The second requirement is ensured with short test times ($\approx 20\,\mathrm{ms}$) available in the Longshot facility.

Pressure sensors (Kulite XCQ-093) with a range of 0.35 to $1.05\,\mathrm{bar}$ are mounted in cavities on the model connected with a $0.8\,\mathrm{mm}$ hole diameter to the surface of the model. The membrane of the sensor is about $1\,\mathrm{mm}$ to the surface of the model. Static calibration of sensors is performed on a weekly basis.

The facility is equipped with a Schlieren system allowing for flow field visualization. For the experiments reported herein, a high speed camera with a sampling rate of $4800\,\mathrm{fps}$ was used with a $800 \times 600\,\mathrm{pixels}$ resolution. The light source was continuous and the exposure time of the camera was set to $15\,\mu\mathrm{s}$, thus being too long to prevent flow disturbances to be recorded.

3.5. Roughness characterization

The flight distributed roughness characteristics resulting from the oxidation process on the nose of the vehicle is currently unknown but will be of statistical nature. In order to represent the disturbances induced to the boundary layer in the wind tunnel, sand elements are stuck to the model. The duplication of roughness characteristics with flight conditions remains an important issue though as sand grain may introduce disturbances different than the ones of on oxidized surface. An example of roughness applied to the model and stuck with varnish spray is given in Fig. 3. The varnish layer is thinner than $0.01\,\mathrm{mm}$. These roughness elements can easily be removed with solvent to test different distributed roughness configuration while using the same model.

Empirical correlations are predicting the critical height of distributed roughness as a single quantity: the roughness height. This single quantity which induces boundary layer transition is particularly difficult to identify and

Test number	T_0 [K]	p_0 [Pa]	Re_L at t=10ms [-]	M_∞ [-]	Roughness mean value $\overline{k}$ [mm]	Roughness standard dev. σ [mm]	Roughness location	Roughness density [1/cm^2]
1627	1610	5.79×10^7	1 740 000	14.0	-	-	-	-
1630	1470	11.09×10^7	3 420 000	14.5	-	-	-	-
1644	1490	11.19×10^7	3 400 000	14.4	0.329	0.066	nose	65
1645	1570	11.04×10^7	3 220 000	14.3	0.329	0.066	subsonic nose	70
1646	1720	10.47×10^7	2 770 000	14.2	0.329	0.066	supersonic nose	70
1647	1630	10.21×10^7	3 120 000	14.2	0.245	0.047	nose	130
1649	1490	11.26×10^7	3 430 000	14.5	0.194	0.038	nose	300
1652	1630	11.75×10^7	3 290 000	14.2	0.194	0.038	nose	130
1653	1580	10.89×10^7	3 030 000	14.2	0.194	0.038	nose	40

Table 1. Test matrix of the experiments performed

as reported in [1, 8], distributed roughness can vary in height, but also width, shape and spacing which are all believe to affect the transition location.

For the current studies, sand grains within a range of interest are obtained from filters. Image analysis is performed in order to check the size distribution of the sand grains. Roughness elements are characterized with their average diameter and the standard deviation from this mean value. Diameters follows a normal distribution whose main value and standard deviation have been reported in Tab. 1. The mean roughness height is considered when compared to the empirical predictions of Sec. 2 although the largest 10 to 20% of all roughness elements are believed to dominate the transition process as mentioned in [8].

Figure 3. Model equipped with roughness $\overline{k} = 0.194$ mm and a density of 300 /cm^2

3.6. Data acquisition procedures and accuracy

Data is acquired at a sampling rate of 500 kHz. Assuming an isentropic and adiabatic flow through the nozzle, and using the reservoir pressure and the stagnation measurements at the nozzle exit, the free-stream quantities are

Quantity	Uncertainty
Reservoir temperature T_0	$\pm 10.0\%$
Mach number M_∞	$\pm 5.0\%$
Reynolds Re_L	$\pm 22.3\%$
corrected Stanton C_H	$\pm 23.1\%$

Table 2. Test conditions uncertainties

rebuilt. The method used based on the Fay-Riddell equation is described in [13]. Uncertainties resulting from this procedure are given in Tab. 2. Stanton number for heat fluxes is determined as $C_H = \dot{Q}/(\rho_\infty u_\infty c_p (T_r - T_w))$ assuming a recovery factor of $r = Pr^{1/2}$ or $r = Pr^{1/3}$ respectively for laminar and turbulent boundary layers [7]. Slight variations of the free-stream Reynolds number between different tests are taken into account using a Stanton number multiplied with the Reynolds number to the power $^1/_2$ or $^1/_3$ [6]. Data presented herein is all relative to $t = 10$ ms from the beginning of an experiment and is averaged over ± 1 ms if not specified otherwise.

4. CFD COMPUTATIONS

Computations have been performed over the EXPERT model in 3D with free-stream conditions matching the ones encountered in the Longshot facility for both laminar and turbulent flows (using compressible Baldwin-Lomax turbulence model). They are used for wall heat flux comparison and to evaluate the critical roughness heights via empirical correlations requiring boundary layers properties.

Additional computations relative to flight conditions have been performed to determine critical roughness heights in flight conditions.

5. RESULTS AND DISCUSSION

5.1. Roughness location variation

Experiments have been initially performed with distributed roughness at different locations on the nose to determine the most effective one to promote transition. Roughness elements ($\bar{k} = 0.329\,\mathrm{mm}$) have been first stuck everywhere on the nose, then in the subsonic part of the nosetip, and finally in the supersonic part as shown in Fig. 4. Corrected Stanton number along the flap side are given in Fig. 5 for the different configurations.
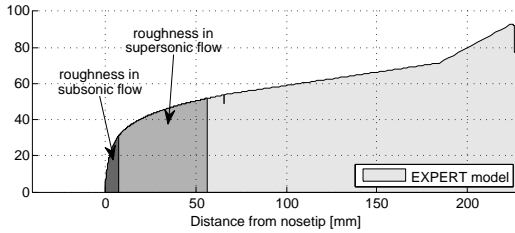
Figure 4. Roughness locations on the nose of the EX-PERT model
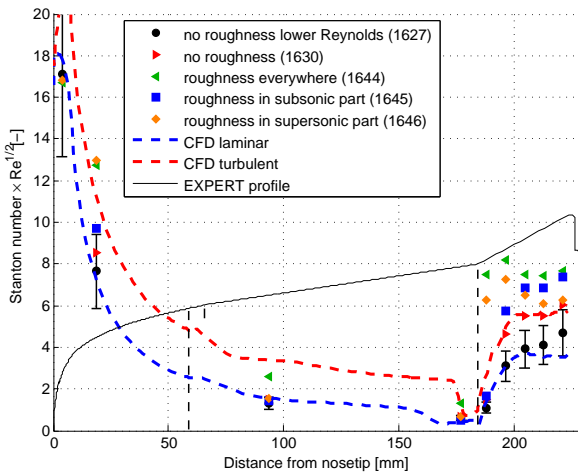
Figure 5. Effect of roughness location on corrected Stanton number along the flap with $\bar{k} = 0.329\,\mathrm{mm}$

Two tests are also reported as smooth references. The first one at a lower Reynolds number matches Stanton number predicted by CFD for a laminar flow over the entire vehicle except at the rear of the flap where a rise departing from CFD predictions depicts a beginning of transition. The second reference test shows a turbulent flow over the flap with an excellent match.

When roughness are present over the entire nose, larger heat fluxes are recorded after the nose but do not reach turbulent predictions. The larger heat transfer rates over the flap may be due to turbulent flow at this location and the overshoot is believed to be due to remaining streamwise flow structures induced by the roughness elements. As noticed in [2], measurements on the nosetip within the roughness elements are not accurate.

For roughness elements located only in the supersonic part of the nose, heat fluxes are kept at a lower level before the flap but increase when reaching it as when roughness is everywhere (for a better match of Stanton numbers with turbulent boundary layer, the exponent used for the Reynolds number correction should be ⅓ [6]).

If roughness elements are located only in the subsonic part, transition still occurs on the flap although the first sensor on the flap records heat fluxes much smaller than before. This is due to the recirculation bubble in front of the flap where the sensor is located, varying in size according to the laminar or turbulent boundary layer as mentioned in [5]. For roughness in the subsonic part only, lower heat fluxes indicate that the first sensor on the flap is located within the recirculation bubble and the boundary layer is thus believed to be laminar. As a consequence, and as already noted in [2] on a similar geometry, roughness elements in the vicinity of the nosetip are not as much efficient to trigger transition. Although the ratio between the roughness elements and the boundary layer thickness is much larger at the nosetip, the strong favorable pressure gradient tends to maintain a laminar flow.

The flow behavior on the model when roughness are everywhere or only in the supersonic part of the nose are similar. Following experiments have been performed with roughness elements over the entire on the nose in order to consider the most destabilizing configuration.

5.2. Roughness height variation

Various sizes of roughness have been applied to the model ($\bar{k} = 0.194\,\mathrm{mm}$, $\bar{k} = 0.245\,\mathrm{mm}$ and $\bar{k} = 0.329\,\mathrm{mm}$). Fig. 7 shows the variation of the Stanton number (corrected for turbulent boundary layers) with different roughness heights along the flap and cone sides. As expected, the largest roughness elements are the most effective ones to trigger transition. For the smaller roughness ($\bar{k} = 0.194\,\mathrm{mm}$) transition is induced on the flap earlier than for the smooth case. For $\bar{k} = 0.245\,\mathrm{mm}$, heat transfer rates are slightly larger along the body but the typical rise of heat transfer for transitional boundary layers is not observed. These larger heat transfer rates might instead be due to streamwise structures issuing from the roughness while the flow is not yet turbulent. For this roughness height, as soon as the flow reaches the flap, larger heat transfer are recorded, depicting the efficiency of the roughness to trigger transition from the flap location. For larger roughness elements ($\bar{k} = 0.329\,\mathrm{mm}$), heat transfer are larger than previously before the flap and similar to the previous case on the flap.

Measurements along the conical side, where there are no stabilizing pressure gradients due to the truncated cone, show similar phenomena: the biggest roughness elements induce the largest wall heat fluxes, close to turbulent CFD predictions. The first sensor records heat fluxes in between the laminar and turbulent CFD predictions and might correspond to a transitional state. Additional
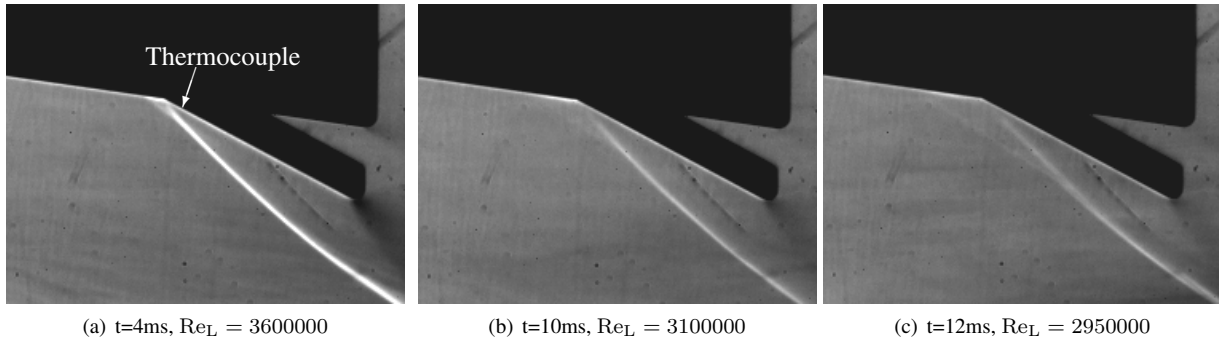
(a) t=4ms, $\text{Re}_L = 3600000$ (b) t=10ms, $\text{Re}_L = 3100000$ (c) t=12ms, $\text{Re}_L = 2950000$

Figure 6. Evolution of the recirculation bubble in front of the flap with decreasing Reynolds number (test 1652)

sensors would have been required to confirm this trend. From the measurements conducted on this side, the critical roughness height to promote transition on the vehicle is estimated to be between $0.194\,\text{mm} < \overline{k} < 0.245\,\text{mm}$ and will be refined in the following sections.
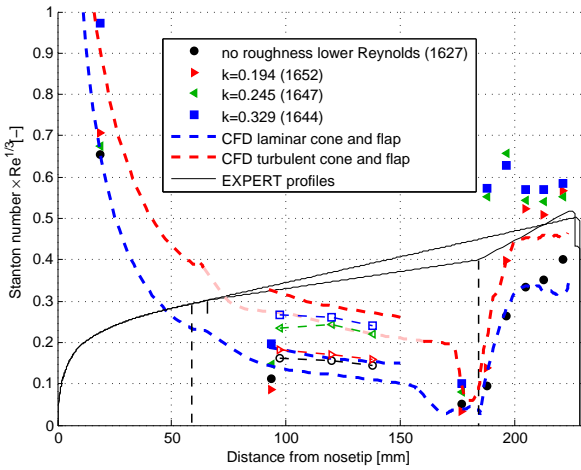
Figure 7. Effect of roughness height on corrected Stanton number along the flap (filled symbols) and the cone (hollow symbols)

5.3. Effects of Reynolds number

This section focuses on test 1652 whose results are considered at different time from the beginning of an experiment while the Reynolds number decreases during an experiment as depicted in Fig. 8. The time required for the flow to travel along the conical side from the nosetip to the end of the model is smaller than $0.3\,\text{ms}$ according to the velocity at the edge of the boundary layer estimated from CFD results. Thus, the flow is considered as being established at each time step over the entire model. Laminar and turbulent flows have been shown to have different behavior in front of an obstacle such as the flap (Sec. 5.1, and [5]). This is observed in the Schlieren pictures of Fig. 6. At the beginning of the experiment, when the Reynolds number is the largest, the flow is turbulent and the recirculation bubble is very narrow (Fig.

6(a)). As the Reynolds number decreases, the boundary layer goes back to its laminar state before the flap and the bubble tend to grow. Shock waves due to separation and reattachment are standing much further apart as visible in Fig. 6(c).
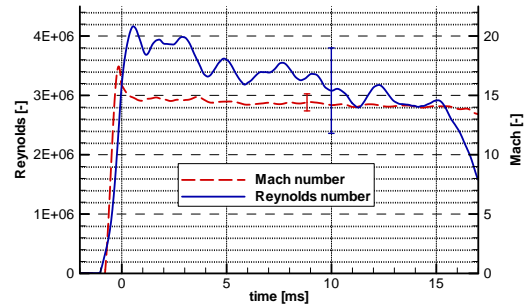

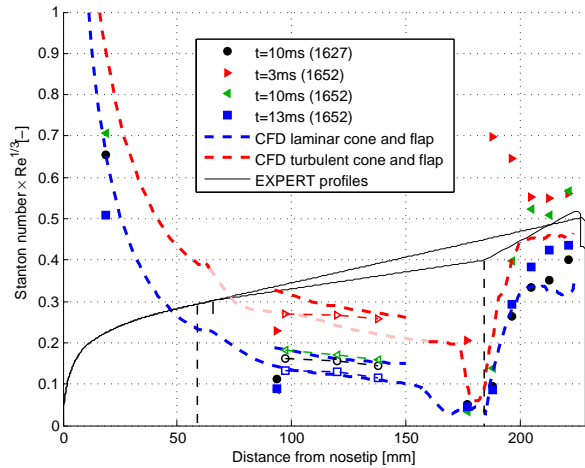*Figure 8. Reynolds and Mach number for test 1652*

Figure 9. Temporal evolution of corrected Stanton number for $\overline{k} = 0.194\,\text{mm}$ along the flap (filled symbols) and the cone (hollow symbols)

A small decrease about 20% in Reynolds number influences significantly the boundary layer. Fig. 9 depicts the evolution of the corrected Stanton number during test 1652. Initially, large heat transfer rates are recorded on the flap before they decrease and until they get close

to the reference laminar case. The difference measured by the first sensor on the flap is particularly interesting and also depicts the evolution of the recirculation bubble. This leads to the conclusion that at $t = 10\,\text{ms}$, while the Reynolds number is close to the one in flight, the boundary layer is in a transitional state.

5.4. Roughness density variation

Different densities of roughness have been applied on the model for $\overline{k} = 0.194\,\text{mm}$. Stanton numbers are reported in Fig. 10. On the flap side, similar heat transfer rates are recorded, being slightly larger for higher densities.
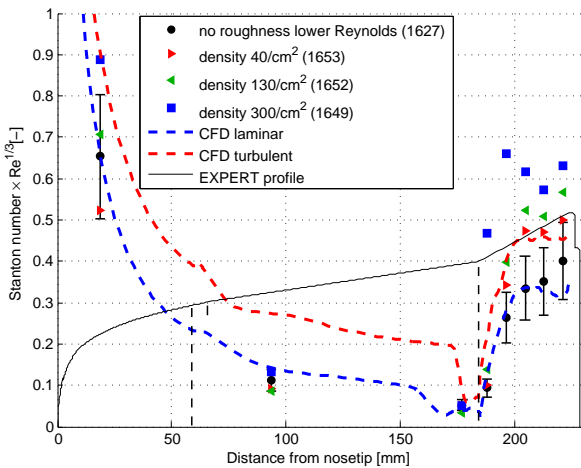
Figure 10. Effect of roughness density on corrected Stanton number along the flap for $\overline{k} = 0.194\,\text{mm}$

The wall heat transfer rates along the cone side deserve to be studied further in this case. The temporal variation of the heat flux recorded at $x = 97.4\,\text{mm}$ along the conical side where stabilizing pressure gradients are limited is given in Fig. 11. The higher the density, the longer turbulent flow is maintained on the model while the Reynolds number is decreasing during a test. This is expected since the amount of disturbances introduced is larger for larger densities. With a density of about 130 elements per cm^2, the boundary layer is in a transitional state at $t = 10\,\text{ms}$ and very close to a laminar state. Therefore, this height is considered as being the critical one inducing transition at $\text{Re}_\text{L} \approx 3\,290\,000$, close to the Reynolds that will occur in flight at Mach 14. Density of the roughness is shown to have a noticeable effect although this parameter is not taken into account in any empirical correlations.

5.5. Prediction of critical heights

By experiments, the critical height to trigger transition along the cone side has been determined to be in the vicinity of $\overline{k} = 0.194\,\text{mm}$. Critical heights predicted by correlations on the nose of the model using CFD results with Longshot conditions are presented in Fig. 12.
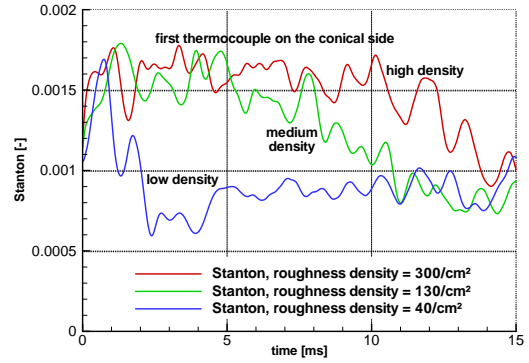
Figure 11. Temporal evolution of corrected Stanton number for a single thermocouple with $\overline{k} = 0.194\,\text{mm}$

The experimental critical height is larger than most of the predictions. Reshotko's, Batt & Legner's, van Driest's correlation and the one of Dirling using a pressure correction term, are predicting smaller critical heights than the one observed experimentally but are in relative good agreement among themselves over the entire nose. This would lead to prefer them for the extrapolation to flight conditions. They are getting closer to the experimental critical value only by the end of the nose. Results from Batt & Legner's correlation are though to be considered carefully after the remarks of Sec. 2. Predictions using PANT and Reda's criteria, lead to critical roughness following another trend. This is due to correlations which are based on boundary layer edge properties instead of local properties at the roughness height. These two correlations are underpredicting the critical roughness height over the whole nose. Predictions using Boudreau's correlation lead to roughness heights much smaller than the other correlations. This is expected since this correlation requires an extension of the roughness zone over 5 times the curvature radius of the nose while in the present configuration, roughness extends for a much shorter distance. Thus, for the present geometry, this correlation should not be used.
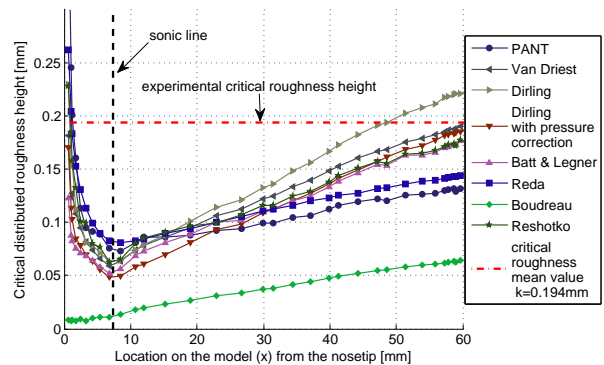
Figure 12. Critical heights predictions for wind-tunnel between nosetip and nose junction

Empirical correlations can predict critical heights for several locations on the model and lead to different results for each of them as they depend upon local flow proper-

ties. In the present case, it is difficult to determine experimentally which zone on the nose has been able to introduce the sufficient amount of disturbances to trigger transition. It is believed all roughness contribute to disturb the flow and especially the ones located in the supersonic part of the nose after the observations reported in Fig. 5. However, within this zone, critical heights predictions still vary with a factor 2 or more.

5.6. Flight extrapolation

An extrapolation to flight conditions is performed using the same empirical correlations. Results are presented in Fig. 13. Predictions by Boudreau's criterion remain lower than the other ones. The previous good agreement observed between the correlations mentioned in Sec. 5.5 is not present anymore. The large scattering of these predictions illustrates the uncertainty remaining in the prediction of the critical roughness height in flight. This scatter might also come from the fact correlations have been based mainly upon wind-tunnel experiments.
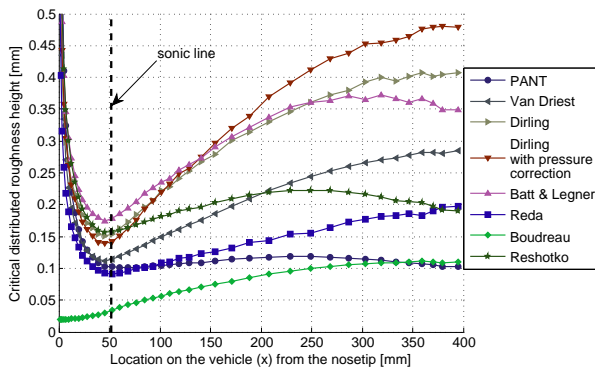

Figure 13. Critical heights predictions for flight at Mach 14 between nosetip and nose junction

6. CONCLUSIONS

Experimental results in the Longshot facility on the EXPERT model have shown the importance of the location over which roughness is located. The roughness extending in the supersonic part of the nose are the most disturbing ones for the boundary layer.

In presence of roughness elements, wall heat fluxes on the flap have been observed to be even larger than the ones obtained on a smooth model with turbulent flow. This is believed to be due to transition phenomena and additional local heating of flow structures induced by the roughness elements.

The density of the roughness elements is a parameter which shall be considered in future studies as it has been shown to be of importance. Large amount of disturbances introduced with high roughness densities has triggered

boundary layer transition while the same roughness with lower density did not disturb the boundary layer.

The critical distributed roughness height determined for the Longshot conditions is about $\bar{k} = 0.194\,\mathrm{mm}$. This is larger than all predictions with empirical correlations varying between $0.049\,\mathrm{mm}$ and $0.221\,\mathrm{mm}$. Each correlation predicts critical heights varying with a factor 2 or more depending on the location of the roughness.

The extrapolation to flight conditions considering van Driest, Dirling and Reshotko's correlations lead to critical heights between $0.115\,\mathrm{mm}$ and $0.481\,\mathrm{mm}$. The large uncertainty remaining is due to the scatter of the empirical predictions and these results are to be carefully considered due to the different conditions and geometries between EXPERT and the ones on which correlations have been developed.

ACKNOWLEDGMENTS

REFERENCES

[1] Batt, R. G. & Legner, H. H. 1983, AIAA Journal, 21, 7

[2] Boudreau, A. H. 1979, Journal of Spacecraft and Rockets, 16, 245

[3] Boudreau, A. H. 1981, Journal of Spacecraft and Rockets, 18, 152

[4] Dirling, R. B., Swain, C. E., & Stokes, T. R. 1975, in AIAA 10th Termophysics conference Denver Colorado No. AIAA paper 1975-673

[5] Kaufman, L. G., Meckler, L., & Hartofilis, S. A. 1966, Journal of Aircraft, 3, 555

[6] Koppenwallner, G. 1984, in Hypersonic aerothermodynamics, LS1984-01 (von Karman Institute)

[7] Korkegi, R. H. 1962, Hypersonic aerodynamics (von Karman Institute)

[8] Reda, D. C. 1981, AIAA Journal, 19, 329

[9] Reda, D. C. 2002, Journal of Spacecraft and Rockets, 39, 161

[10] Reshotko, E. & Tumin, A. 2004, AIAA Journal, 42, 766

[11] Schneider, S. P. 2008, Journal of Spacecraft and Rockets, 45, 641

[12] Schneider, S. P. 2008, Journal of Spacecraft and Rockets, 45, 193

[13] Simeonides, G. 1990, The VKI hypersonic wind tunnels and associated measurement techniques, Technical Memorandum 46, von Karman Institute